International Journal of Ceramic Engineering & Science

RESEARCH ARTICLE OPEN ACCESS

Finite Element Analysis of *R*-Curve Behavior in Ceramics Using the Damage Model Based on the Cohesive-Zone Relationship

Mostafizur Rahman[1,2] | Taiyo Maeda[1] | Toshio Osada[3,4] | Shingo Ozaki[3,4]

[1]Graduate School of Engineering Science, Yokohama National University, Yokohama, Japan | [2]Department of Mechanical Engineering, Chittagong University of Engineering & Technology (CUET), Chattogram, Bangladesh | [3]High-Reliability Heat-Resistant Materials Group, Research Center for Structural Materials, National Institute for Materials Science, Tsukuba, Ibaraki, Japan | [4]Division of System Research, Faculty of Engineering, Yokohama National University, Yokohama, Japan

Correspondence: Shingo Ozaki (s-ozaki@ynu.ac.jp)

Received: 16 June 2025 | **Revised:** 15 August 2025 | **Accepted:** 1 September 2025

Funding: This work is based on results obtained from a project, JPNP22005, commissioned by the New Energy and Industrial Technology Development Organization (NEDO). Part of this study was supported by Grant-in-Aid for Scientific Research [Grant (B) 22H01357], Japan Society for the Promotion of Science (JSPS).

Keywords: ceramics | damage model | finite element analysis | *R*-curve behavior | toughness

ABSTRACT

The evaluation of the *R*-curve behavior of ceramics, which is characterized by an increase in crack resistance with crack propagation, is crucial for advancing their implementation in engineering applications that require high reliability. In this study, we investigated the applicability of a finite element analysis (FEA) approach that implements a continuum damage model embedded with a cohesive-zone relationship to predict crack occurrence and the subsequent increase in crack resistance (toughness) of ceramics. Specifically, by employing a compliance-based method, the *R*-curve behavior was systematically examined under a bending load to assess the impacts of fracture stress and toughness on diverse chevron-notched specimens. The output critical stress intensity factors were found to increase with the crack length, eventually converging nearly to the input fracture toughness. Subsequently, the stable crack growth behavior obtained from the FEA and experiment under a three-point bending test of high-purity alumina was compared. A consistent result was confirmed in the force–displacement relationships. Furthermore, the *R*-curve behavior of the target material could be indirectly evaluated using the present approach. The results support the effectiveness of the present approach, highlighting the quantitative assessment of not only crack initiation but also *R*-curve behavior under arbitrary boundary conditions.

1 | Introduction

Ceramics have recently garnered attention for structural applications owing to their exceptional mechanical properties, including lightness, thermal resistance, and high specific strength [1–4]. These properties, coupled with their resistance to wear and corrosion, make ceramics ideal for a wide range of applications, such as aerospace, energy generation, automotive, and electronics [5–11]. However, to ensure reliability and safety in sophisticated engineering applications, comprehensively investigating the fracture behavior of ceramics is crucial. This investigation is key to optimizing the microstructure and shape of ceramics to enhance their fracture resistance and achieve controlled stable crack growth [12–14]. This is important, as rapid and

catastrophic crack growth can result in sudden failure, which decreases the reliability and integrity of ceramic structural components [15, 16].

Fracture toughness, especially the *R*-curve behavior, which is characterized by an increase in crack resistance with crack propagation, is important for assessing the resistance of ceramics to the crack growth rate. Although the fracture toughness offers a single-value measure of this resistance, the *R*-curve provides a more dynamic and comprehensive perspective; it illustrates the evolution of the fracture resistance with increasing crack length [17]. Toughening mechanisms, such as crack deflection, crack bridging, and interlocking, contribute to the enhancement of fracture resistance, resulting in a rising-type *R*-curve [18]. Becher et al. [19, 20] investigated these mechanisms and the improvements in the fracture toughness of alumina- and mullite-based ceramics.

Although previous experimental approaches explored the micro mechanisms responsible for toughening, they often lacked a detailed analysis of the *R*-curve behavior. Despite the significance of the *R*-curve analysis, studying these behaviors in ceramics presents several challenges, including the need for precise experimental techniques to measure the stress intensity factor (SIF) and accurately track the crack growth. Advances in experimental methods, such as digital image correlation (DIC) and in situ mechanical testing, have simplified the study of *R*-curve behavior, as demonstrated by Grutzik et al. [21]. They analyzed the *R*-curve behavior in glass- and Si_3N_4-based ceramics under four-point bending (4PB) test conditions.

However, many early attempts have primarily focused on improving fracture stress and toughness by optimizing microstructural features, manufacturing techniques, and testing methods. To evaluate the *R*-curve behavior and promote the application of ceramics, integrating the experimental and numerical approaches is essential. Finite element analysis (FEA) approach is one of the leading candidates of simulation methods for assessing not only crack initiation but also following the crack growth under arbitrary boundary conditions. Furthermore, FEA enables a detailed analysis of stress distribution and SIF with crack growth through the fractured surface and ahead of the crack tips. Thus, it provides a deeper insight into the fracture process, which is difficult to achieve experimentally alone, especially in complex geometries. In addition, FEA facilitates the evaluation of stable crack growth and enables the exploration of the influence of the diverse conditions on the *R*-curve behavior.

In this study, the effectiveness of the FEA approach to predict crack occurrence, followed by an increase in the crack resistance (toughness) of ceramics, was investigated. In the FEA approach, a continuum damage model with an embedded cohesive-zone relationship was implemented [22]. Specifically, the *R*-curve behavior of diverse chevron-notched specimens subjected to bending loads was examined, which was designed to induce stable crack growth. First, *R*-curve analyses for various fracture properties, specimen geometries, and test conditions were systematically performed using the compliance-based method. Subsequently, the experimental results of three-point bending (3PB) tests using chevron-notched alumina ceramics were compared with the FEA simulations. Then, using the FEA results corresponding to the experiment, we investigated the feasibility of the approach to examine the *R*-curve behavior in detail, even with systems in which experimental measurements related to stable crack growth behavior are difficult.

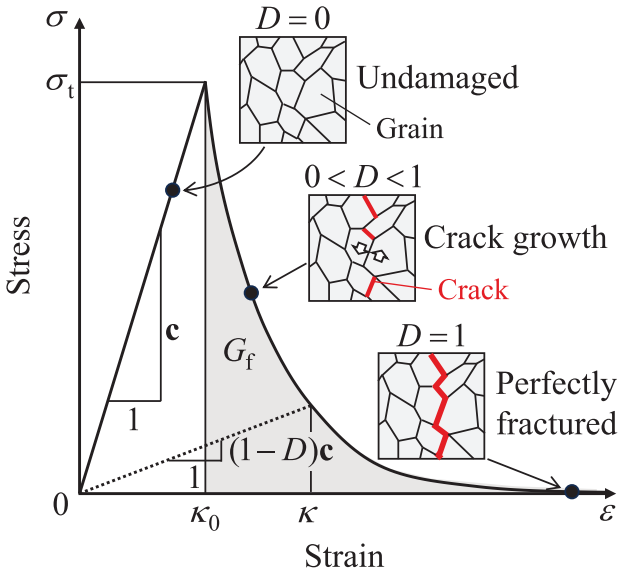

FIGURE 1 | Typical stress–strain relationship in the isotropic constitutive damage model [23–25]. The fracture stress is assumed to decrease exponentially with the crack growth.

2 | Continuum Damage Model

An isotropic damage model based on fracture mechanics [22] was adopted to analyze the *R*-curve behavior of brittle ceramics. The stress–strain relationship between the Cauchy stress tensor σ and infinitesimal strain tensor ε can be written as follows:

$$\boldsymbol{\sigma} = (1 - D)\,\mathbf{c} : \boldsymbol{\varepsilon}, \tag{1}$$

where c and D represent the fourth-order elastic modulus tensor and damage variable, respectively. The damage variable D ranges from 0 to 1, indicating the degree of damage, with 0 corresponding to the undamaged state and 1 corresponding to the perfectly fractured state, as shown in Figure 1 [23–25].

To describe the damage process in brittle materials, the cohesive force-crack opening relationship (Equation 2) was incorporated into the damage model:

$$\sigma = \sigma_t \exp\left(-\frac{\sigma_t}{G_f} w\right), \tag{2}$$

where σ is the cohesive force per unit area, σ_t is the local fracture stress, G_f is the fracture energy, and w is the crack opening displacement. Equation (2) can be rearranged in the same form as Equation (1) [22]. Thus, the damage variable D can be expressed as follows:

$$D(\kappa) = 1 - \frac{\kappa_0}{\kappa} \exp\left\{-\frac{\sigma_t h_e}{G_f}(\kappa - \kappa_0)\right\}, \tag{3}$$

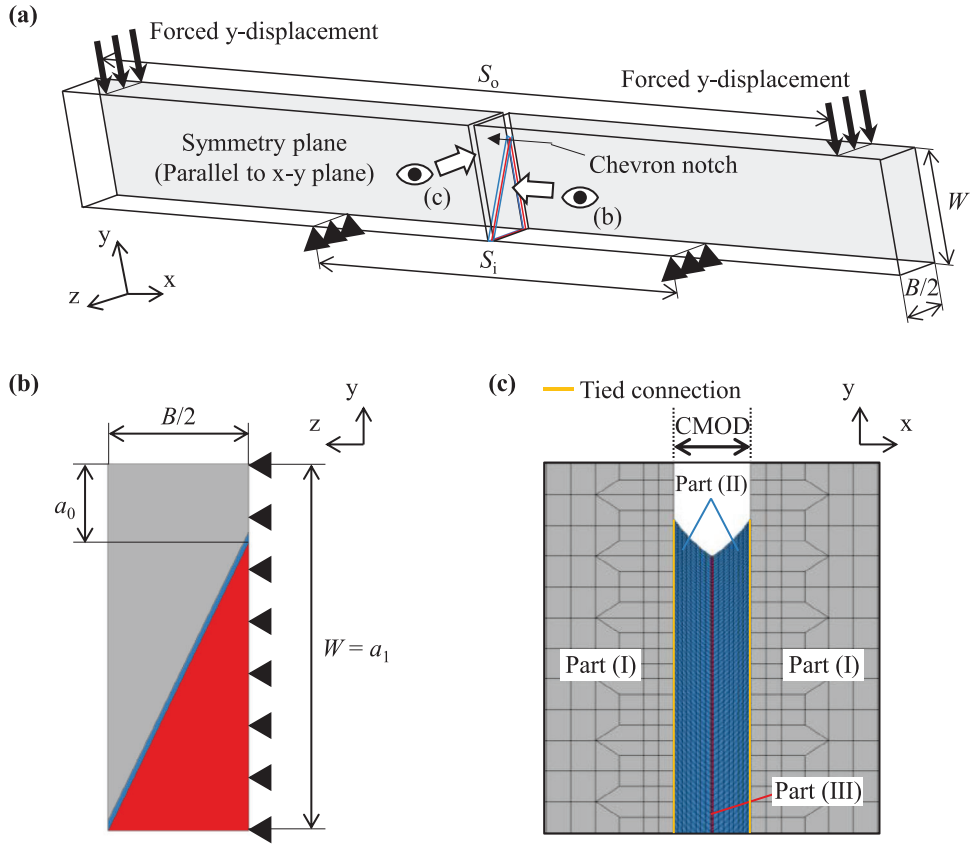

FIGURE 2 | FEA model for 3PB and 4PB test: (a) generalized view of dimensions and constraint conditions; (b) dimensions and constraint conditions from the right side view of (a); (c) a close-up view around the chevron notch area. Here, the model is symmetric in the *z*-direction. As shown in the close-up view around the damaged part in the notch tip, the crack propagates through the center Part (III), as indicated by the red elements.

where h_e the characteristic length (i.e., the length in the crack opening direction of the unit element used in the FEA) [26]. κ is the damage history variable, which is the internal variable of the damage variable and corresponds to the maximum equivalent strain in loading history. As this study was focused on Mode I fracture behavior of ceramics, the local fracture stress σ_t (the fracture criterion) was evaluated on the basis of the maximum principal stress. Further, the equivalent strain when the maximum principal stress reaches the local fracture stress was adopted for κ_0 [23–25].

3 | FEA of *R*-Curve Behavior

3.1 | FEA Model

The FEA of the *R*-curve behavior and stable crack growth was performed using chevron-notched specimen models, following the American Society for Testing and Materials (ASTM) standard [27]. The commercial software package LS-DYNA [28] was used in the FEA, and the damage model was implemented using the user subroutine *umatXX*. FEA was performed using the dynamic explicit method and mass scaling. In this study, the applicability of FEA based on the continuum damage model to the *R*-curve behavior of ceramics was examined under various geometries and loading conditions, as well as the material properties of chevron-notched specimens. The FEA models used for the bending test analyses are shown in Figure 2 and their dimensions are listed in Table 1. Here, according to the ASTM standard, configurations A, D, and B were used for the 4PB and 3PB tests, respectively. The bending tests were performed by applying forced displacements and constraint conditions to specific nodes, as shown in Figure 2a. Figure 2b shows a cross-sectional view of the notched area in the *x*-positive direction (Figure 2a). The model was halved using the *x*–*y* plane shown (Figure 2a) as the symmetry plane to reduce the computational cost.

The FEA model consisted of three parts: Part (I), the smooth part; Part (II), the lower side of the notch; and Part (III), the lower center of the notch. Although the same Young's modulus and Poisson's ratio were input for all parts, the linear elastic model was applied as the material model in Parts (I) and (II). This is because fracture did not occur at these locations owing to the stress concentration at the notch tip. The damage model was applied to Part (III). Figure 2c shows the area around the notch tip viewed from the positive *z*-direction (Figure 2a). Tied contacts were used as the nodal coordinates did not overlap at the interface between Parts (I) and (II) [28]. In addition, the notch tip was modeled with a curvature formed assuming drilling machining, which enabled the behavior of stable crack growth from the center of the notch tip to be reproduced in the experiments (Section 5). To reproduce a stable crack growth in FEA, the element size, particularly in the crack propagation zone, is important. In this study, the most focused was Part (III) with the damage model, featuring a unit element size of 5.95 μm (=h_e). The mesh sizes in Parts (I)–(III) were different, as shown in Figure 2.

TABLE 1 | Specimen and test geometries of three-point bending (3PB) and four-point bending (4PB) tests.

Configuration	B [mm]	W [mm]	a_0 [mm]	S_i [mm]	S_o [mm]
ASTM A	3.2	4.2	0.87	20	40
ASTM B	6.4	6.4	2.54	0	20, 30, 40
ASTM D	3.2	4.2	1.47	20	40

Abbreviation: ASTM, American Society for Testing and Materials.

TABLE 2 | Basic material properties of alumina ceramic (AS999).

Young's modulus	Poisson's ratio	Density
E [GPa]	ν [−]	ρ [kg/m^3]
380	0.24	3950

The basic material properties of the alumina-based ceramics are listed in Table 2. Two variations of fracture properties, local fracture stress σ_t and fracture toughness K_{IC}, were prescribed as follows: Type (i) σ_t = 890 MPa with K_{IC} = 4.0, 8.0, and 12.0 MPa m$^{0.5}$; and Type (ii) σ_t = 450 MPa with K_{IC} = 3.0, 6.0, and 9.0 MPa m$^{0.5}$. These properties were approximately identical to those of alumina reinforced with silicon carbide particles, alumina reinforced with silicon carbide whiskers, nacre-like alumina with silicon carbide whiskers, pure alumina, and nacre-like alumina [29–32].

3.2 | Evaluation of *R*-Curve Behavior

In this study, a compliance-based method was adopted to evaluate the *R*-curve behavior of ceramics. The *R*-curve represents the SIF obtained as a function of crack length in the stable fracture process of a notched specimen [33]. The critical SIF before full fracture is termed as the Mode I fracture toughness, K_{IC} [34]. Here, the fracture toughness can be determined using the maximum value of the bending load, geometric condition of the specimen, crack size, and rate of change of the dimensionless compliance with the crack length, without information on the *R*-curve [35]. The SIF for mode I, K_I, under the plane strain condition is expressed as follows [34, 36]:

$$K_I = \sqrt{\frac{EG_I}{1-\nu^2}}, \tag{4}$$

where E is the Young's modulus, ν is the Poisson's ratio, and G_I is the energy release rate. When a bending load p is applied in the 3PB or 4PB test on a chevron-notched specimen (Figure 3a), the energy release rate for the chevron crack (Figure 3b) is given by [36]

$$G_I = \frac{p^2}{2b}\frac{dC}{da}, \tag{5}$$

where b is the crack-tip width, C is the compliance, and a is the crack length. On the basis of the geometry of the chevron notch (Figure 3b), the crack-tip width b is given by

$$b = \frac{a-a_0}{a_1-a_0}B, \tag{6}$$

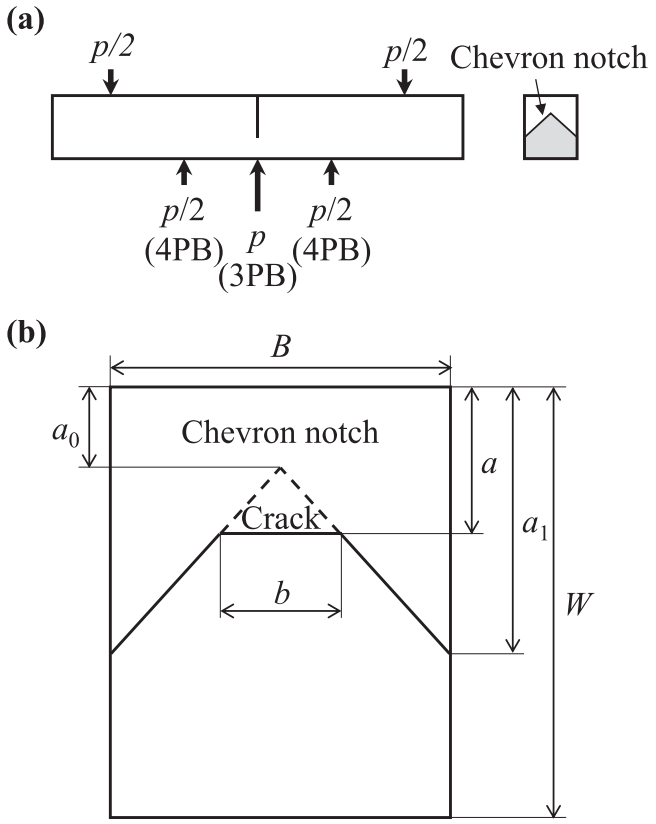

FIGURE 3 | Schematic of chevron-notched specimen in analysis: (a) 3PB and 4PB test model; (b) cross-sectional shape of test specimen. 3PB, three-point bending; 4PB, four-point bending.

where B is the specimen width, a_0 is the pre-crack length to the tip, and a_1 is the pre-crack length at the edge. Therefore, K_I can be written by arranging Equations (4–6) as follows:

$$K_I = \frac{p}{B\sqrt{W}}\sqrt{\frac{1}{2}\frac{\alpha_1-\alpha_0}{\alpha-\alpha_0}\frac{dC'}{d\alpha}}, \tag{7}$$

where W is the thickness of a specimen, C' (=CBE/(1 − ν^2)) is the dimensionless compliance, and α (=a/W) is the dimensionless crack length. In the FEA, the crack length is the sum of the element lengths in the direction of crack growth, where the element damage variable $D > 0.05$.

4 | FEA Results of *R*-Curve Behavior

We investigated the *R*-curve behavior of ceramics by inducing a >3-mm-length crack through the chevron notch part by utilizing the prescribed fracture properties. Furthermore, the occurrence

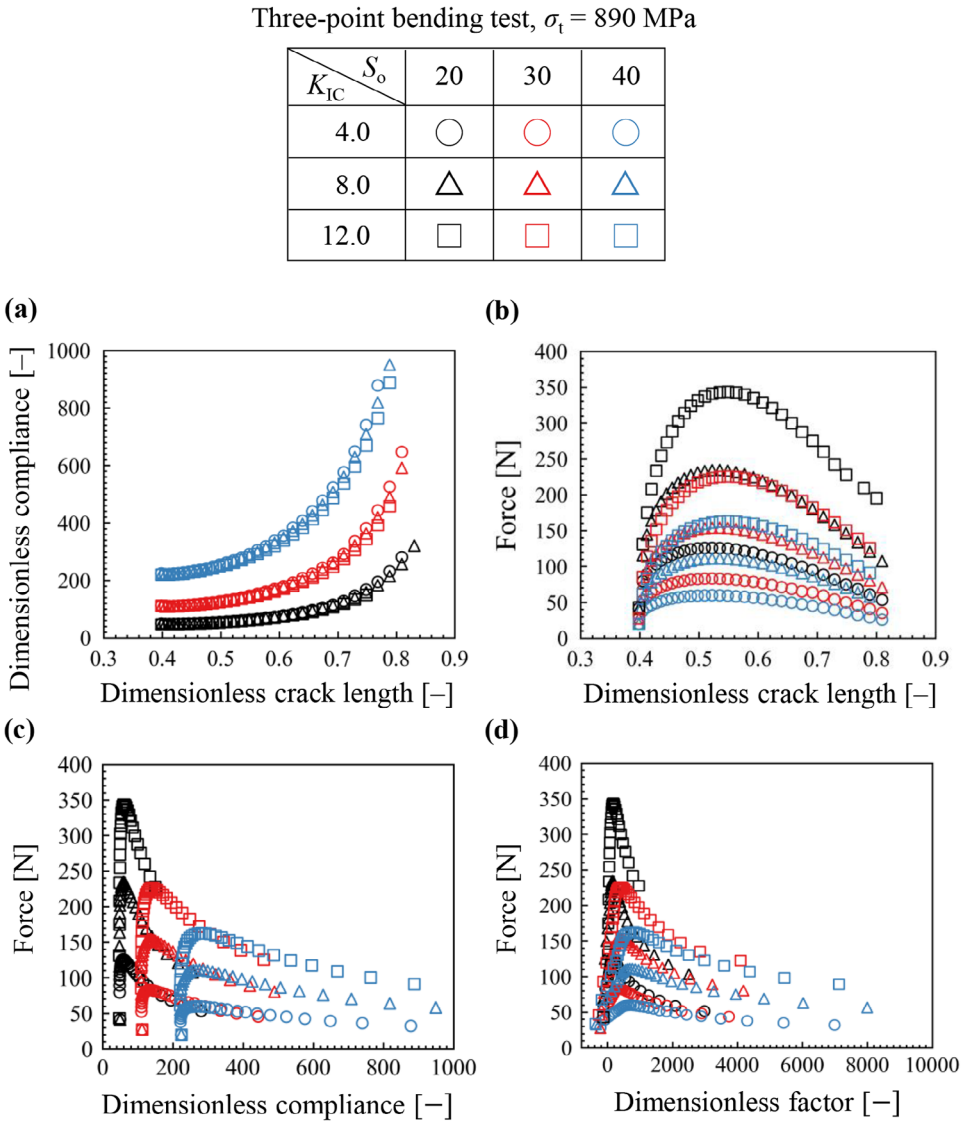

FIGURE 4 | FEA results from fracture toughness K_{IC} [MPa $m^{0.5}$] variation under the 3PB test for ASTM B specimens: (a) change in dimensionless compliance with dimensionless crack length; (b) change in reaction force with dimensionless crack length; (c) change in reaction force with dimensionless compliance; (d) change in reaction force with change in dimensionless factor. Here, the outer span length (S_o) is 20, 30, and 40 mm, and fracture stress (σ_t) of 890 MPa is maintained constant for all cases.

of stable crack growth during the fracture process of ceramics using FEA was evaluated.

4.1 | Chevron-Notched ASTM Model for 3PB Test

Figure 4 shows the FEA results obtained by 3PB tests (outer span lengths S_o = 20, 30, and 40 mm) following the ASTM B configuration (Table 1). Here, the input fracture properties were of Type (i). Figure 4a shows the relationship between the dimensionless compliance and dimensionless crack length. Regardless of the fracture toughness values, the dimensionless compliance increased in the same manner as the crack length, leading to similar crack growth. The obtained behavior resembled the reported experimental results for coarse-grained alumina obtained by adopting several test approaches [37, 38]. Conversely, the compliance depends on the outer span length S_o, influenced by the effective stress concentration area. This consistency suggests the validity of the fracture behaviors obtained by FEA and calculated using the compliance-based method.

Furthermore, the change in the reaction force with the dimensionless crack length indicated that the force increased gradually with the crack growth and even decreased progressively after the crack reached a certain region in the chevron notch area, as shown in Figure 4b. This is because the material no longer showed resistance to crack growth as the crack growth rate increased. Notably, the higher the fracture toughness value and the smaller the outer span length, the larger the peak reaction force, which was confirmed to induce almost the same level of crack length. Figure 4c,d illustrates the changing tendencies of different peak reaction forces with respect to the changes in the dimensionless compliance and dimensionless factor, respectively. Here, the dimensionless factor is denoted as the ratio between the increments of dimensionless compliance and dimensionless

Three-point bending test, σ_t = 890 MPa

K_{IC} \ S_o	20	30	40
4.0	○	○	○
8.0	△	△	△
12.0	□	□	□

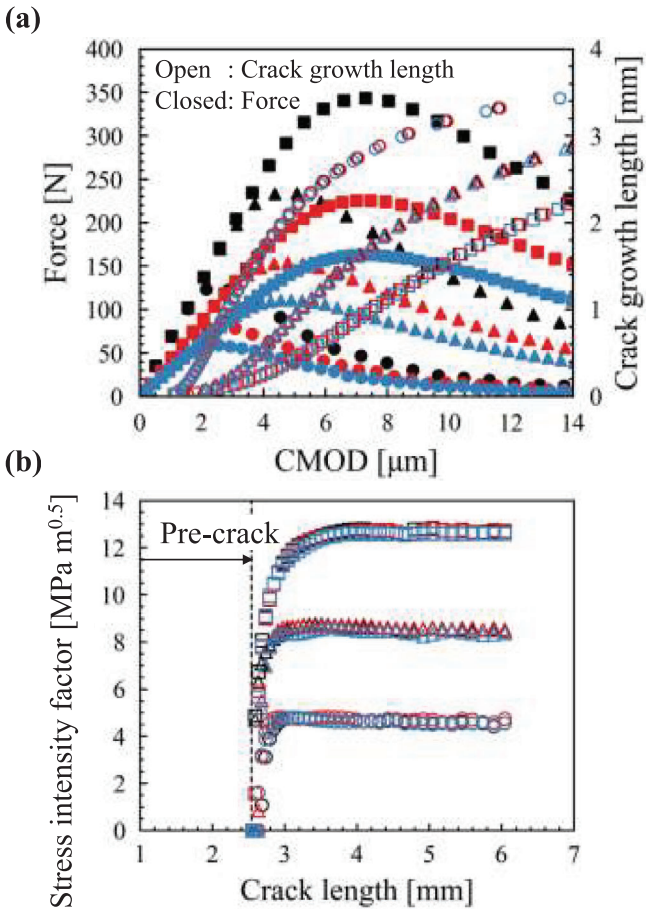

FIGURE 5 | FEA results from fracture toughness K_{IC} [MPa $m^{0.5}$] variation under the 3PB test for ASTM B specimens: (a) comparison of force–CMOD and crack growth length–CMOD relationships; (b) comparison of *R*-curves. Here, the outer span length (S_o) is 20, 30, and 40 mm, and fracture stress (σ_t) of 890 MPa is maintained constant for all cases. CMOD, crack mouth opening displacement.

Three-point bending test, σ_t = 450 MPa

K_{IC} \ S_o	20	30	40
3.0	○	○	○
6.0	△	△	△
9.0	□	□	□

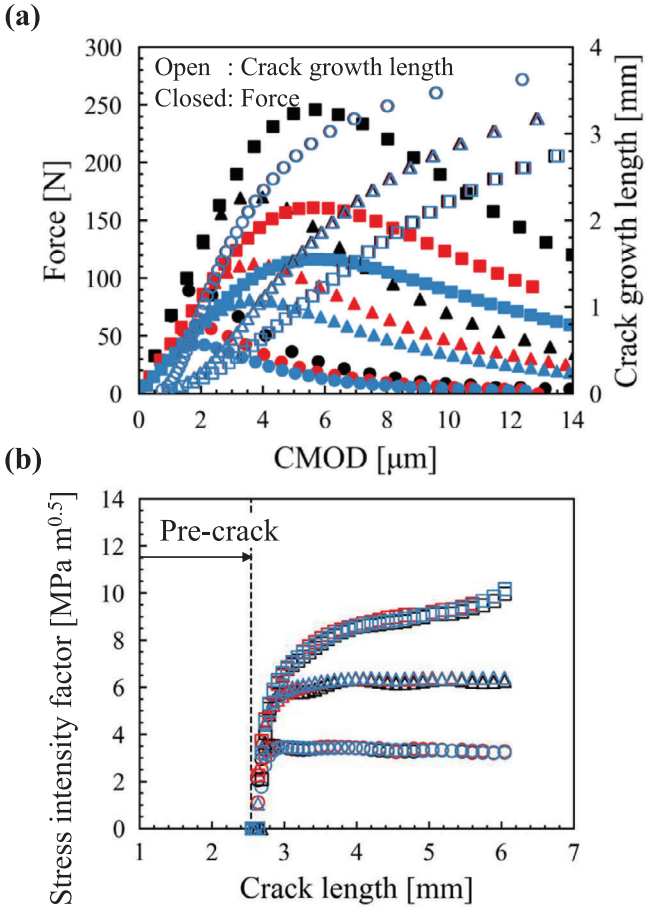

FIGURE 6 | FEA results from fracture toughness K_{IC} [MPa $m^{0.5}$] variation under the 3PB test for ASTM B specimens: (a) comparison of force—CMOD and crack growth length—CMOD; (b) comparison of *R*-curves. Here, the outer span length (S_o) is 20, 30, and 40 mm, and fracture stress (σ_t) of 450 MPa has been kept fixed for all cases. CMOD, crack mouth opening displacement.

crack length (=$\Delta C'/\Delta\alpha$). The reaction force initially increased with dimensionless compliance and thereafter decreased in a likely exponential manner, following almost the same line when the fracture toughness was the same, even when the outer span length was varied.

Figure 5a shows the variations in the reaction force and crack growth length with respect to the crack mouth opening displacement (CMOD; Figure 2c). Even after crack initiation, the force increased gradually up to a peak with the CMOD and decreased stably after the peak force as the crack growth rate increased gradually. As the crack initiation force of ceramics is dominated by the local fracture stress [39], cracks initiate at the same CMOD and reaction force, even for a different fracture toughness. Furthermore, the crack initiation force depending on the test condition was estimated to be 44, 29, and 21 N for outer span lengths of 20, 30, and 40 mm, respectively. However, the crack growth rate is significantly influenced by the fracture toughness; the higher the fracture toughness, the smaller the crack growth length with respect to the CMOD. Furthermore, the crack growth rate was identical regardless of the outer span length when the input fracture toughness was the same. These fracture behaviors are reflected in the *R*-curve (Figure 5b). Initially, the SIF increased with the crack growth and converged to almost the same values as the respective input fracture toughness after the crack reached a certain length in the chevron notch. Mesh size discretization may cause a slight discrepancy between the input fracture toughness value and the output SIF from the FEA.

Three-point bending test, σ_t = 890 MPa

K_{IC}	ASTM A	ASTM D
4.0	○	○
8.0	△	△
12.0	□	□

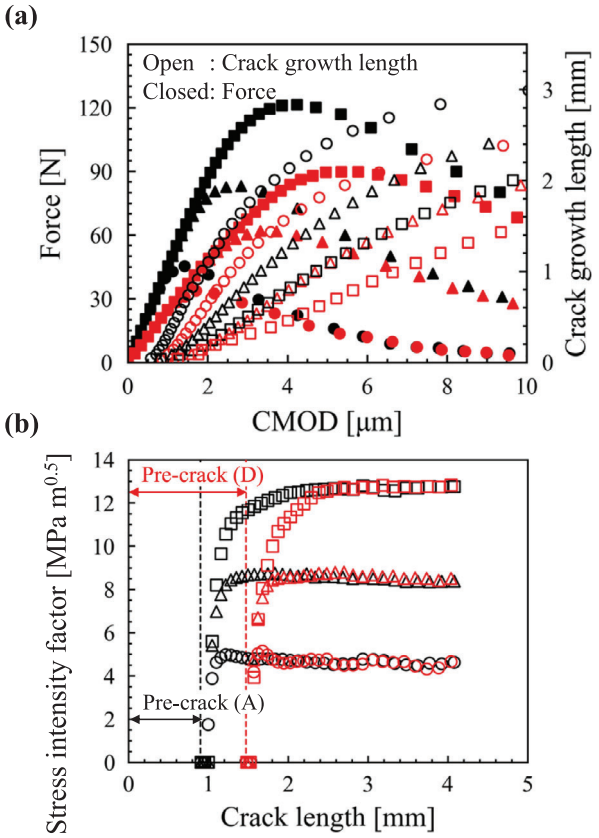

FIGURE 7 | FEA results from fracture toughness K_{IC} [MPa $m^{0.5}$] variation under 4PB test: (a) comparison of force–CMOD and crack growth length–CMOD relationships; (b) comparison of *R*-curves. Here, the inner span length (S_i) and the outer span length (S_o) are 20 and 40 mm, respectively, and the fracture stress (σ_t) of 890 MPa is maintained constant for all cases. CMOD, crack mouth opening displacement.

Three-point bending test, σ_t = 450 MPa

K_{IC}	ASTM A	ASTM D
3.0	○	○
6.0	△	△
9.0	□	□

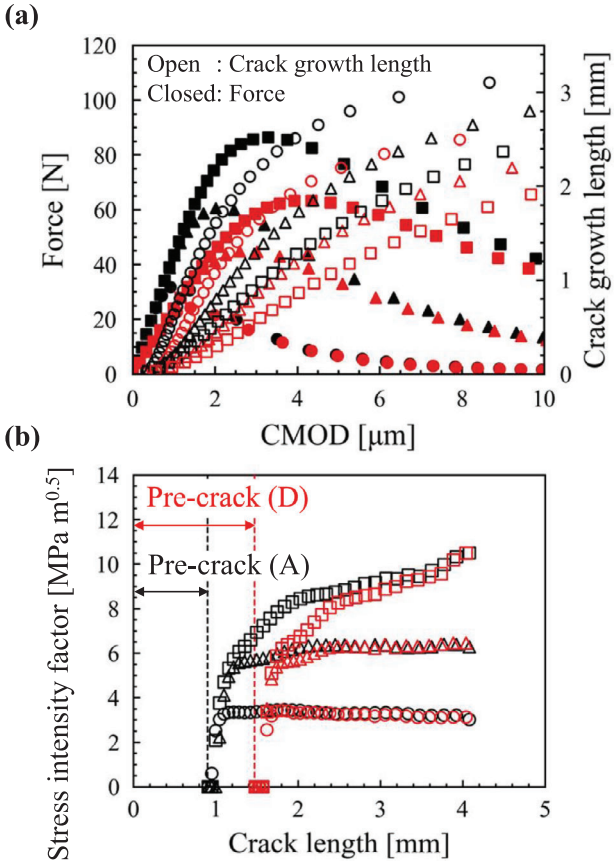

FIGURE 8 | FEA results from fracture toughness K_{IC} [MPa $m^{0.5}$] variation under 4PB test: (a) comparison of force–CMOD and crack growth length–CMOD relationships; (b) comparison of *R*-curves. Here, the inner span length (S_i) and the outer span length (S_o) is 20 and 40 mm, respectively, and the fracture stress (σ_t) of 450 MPa is maintained constant for all cases. ASTM, American Society for Testing and Materials; CMOD, crack mouth opening displacement.

The shapes and slopes of the *R*-curve obtained by FEA were significantly dependent on the input fracture energy G_f calculated from the fracture toughness K_{IC} and basic material properties (Table 2). This trend was experimentally demonstrated by considering several grades of ceramics [40–43]. Therefore, the effects of the fracture properties on the fracture and *R*-curve behavior (Figure 6) were investigated. The effect of the variation in fracture properties (i and ii) can be illustrated by comparing Figures 5a and 6a. The crack initiation force, peak reaction force, and crack growth behavior were significantly dependent on the input fracture properties. The crack initiation forces were estimated to be 24, 15, and 11 N for outer span lengths of 20, 30, and 40 mm, respectively, for fracture property type (ii) (Figure 6a).

Output SIFs converged and nearly equalized to input values at K_{IC} = 3.0 and 6.0 MPa $m^{0.5}$ (Figure 6b). These two behaviors appeared as flat-type *R*-curves, similar to those reported by Bleise and Steinbrech [44], who adopted coarse-grained alumina to experimentally produce long cracks. In contrast, the output SIF did not converge and was slightly higher than the input value at K_{IC} = 9.0 MPa $m^{0.5}$. This behavior can be treated as a rising-type *R*-curve [41, 45, 46], which was experimentally observed in highly toughened bioinspired nacre-like alumina [31] and silicon nitride [45], the fracture stress and toughness values of which were measured to be almost identical to the values input into FEA. These findings highlight the effectiveness of the present FEA approach for analyzing the fracture and *R*-curve behaviors of ceramics.

In situ experimental observations, including crack deflection, crack branching, bridging, microcracking, and delamination,

were conducted in the single-edge notched bending test, which caused the rising-type *R*-curve behavior. This phenomenon was also observed by many researchers when investigating improvements in the mechanical properties of different ceramic-based brittle materials [47–53]. Therefore, the causes of the rising-type behavior in FEA indirectly reflected the effects of the experimental toughening mechanisms, that is, crack deflection, crack branching, bridging, microcracking, and delamination. These toughening mechanisms significantly affect crucial fracture parameters, such as reactive force and dimensionless compliance, under variations in fracture properties. Hence, the integration of the changes in the fracture parameters and their substitution into Equation (7) reflect the flat and rising-type *R*-curve behaviors according to the fracture properties.

4.2 | Chevron-Notched ASTM Model for 4PB Test

The fracture and *R*-curve behaviors using the fracture properties (i) and (ii) under the 4PB test adopting configurations A and D (Table 1) were evaluated to examine the occurrence of stable crack growth. The only distinction between these configurations was the pre-crack length, whereas the other geometries and constraint conditions were identical to those shown in Figure 2. Figure 7 shows the relationships of force and crack growth length with the CMOD and the corresponding *R*-curve behavior for both configurations A and D for fracture property type (i). The difference in the pre-crack length between the configurations caused variations in the crack initiation force, peak force, and crack growth length, as shown in Figure 7a. The crack initiation force was estimated to be 15 and 11 N for configurations A and D, respectively. In addition, the slopes of the force and CMOD curves changed owing to the difference in the stress concentration area through the chevron notch. The peak force induced in configuration A (shorter pre-crack length) was estimated to be higher than that in configuration D (longer pre-crack length) to generate the same level of CMOD. Furthermore, the changes in the crack growth length with the CMOD of configuration A were greater than those of configuration D. To investigate the convergence and coherency, these results were reflected in the *R*-curve behavior (Figure 7b). The SIFs increased with increasing crack length and converged when the crack reached a certain length into the chevron notch. Type (i) fracture properties output a flat *R*-curve behavior [44] from both configurations under the 4PB test conditions.

The impacts of the fracture properties (Types (i) and (ii)) are shown in Figures 7 and 8 for both configurations. Collectively, these results correspond to stable crack growth in the stable fracture process of ceramics, which is similar to the stable crack growth and corresponding *R*-curve behavior of the ZrB_2/SiC ceramic composite reported by Lugovy et al. [54] at room temperature using the V-notched specimens in the 4PB test.

4.3 | Comparison of *R*-Curve Behaviors Between 3PB and 4PB Tests

Figure 9 illustrates the changes in SIF with the crack growth length between the 3PB test (ASTM B) and 4PB test (ASTM A and D) under fracture property type (i). Noteworthy, the relationships

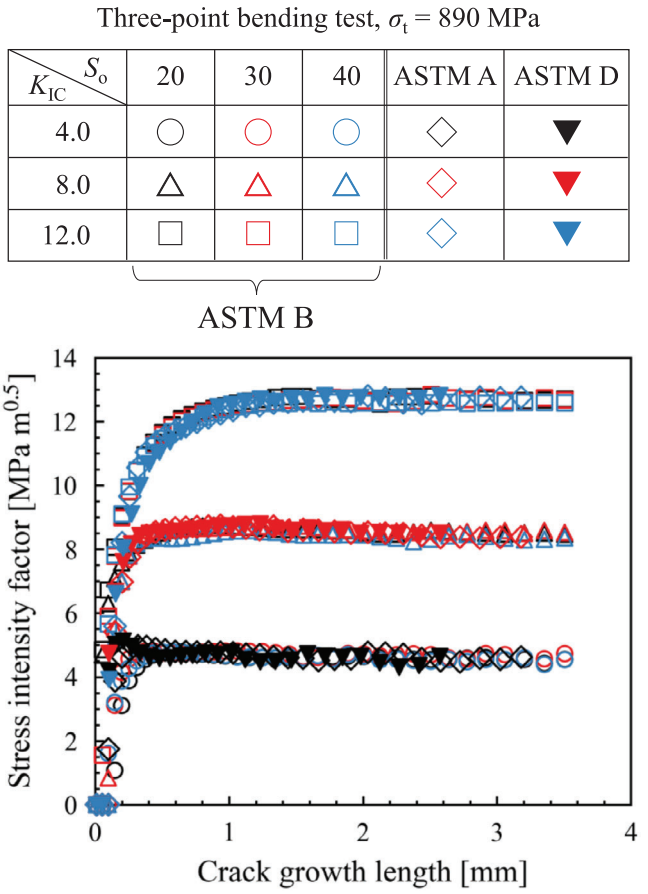

FIGURE 9 | Comparison of *R*-curve behaviors between 3PB and 4PB tests adopting fracture properties type (i). Here, the fracture toughness K_{IC} [MPa m$^{0.5}$] was varied, whereas the fracture stress (σ_t) of 890 MPa was maintained constant for all cases. ASTM, American Society for Testing and Materials.

between SIF and crack growth length were independent of specimen geometries and test conditions, indicating a similar trend of stress distribution over the fractured surface and ahead of crack tip. Furthermore, this type of independence was also observed for fracture property type (ii) (Figure 10). However, a slight deviation was observed in the 4PB tests at K_{IC} = 9.0 MPa m$^{0.5}$, probably owing to the difference in specimen geometries and random stress–toughness trade-off (Figure 10). Moreover, in this case, the peaks of the SIF corresponding to the maximum crack growth length were approximately identical for the specimen geometries. The SIF was quantified with the crack growth length, depending on the nature of the fracture toughness of the ceramics (Figures 9 and 10). These results highlight the effectiveness of the proposed FEA approach for evaluating the fracture initiation and subsequent *R*-curve behavior of ceramics under diverse test conditions that induce stable crack growth.

5 | Comparison Between FEA and Experiment

5.1 | Experiment

High-purity alumina AS999 (Ferrotec Material Technologies Corporation, Japan) was used in the experiment. It should

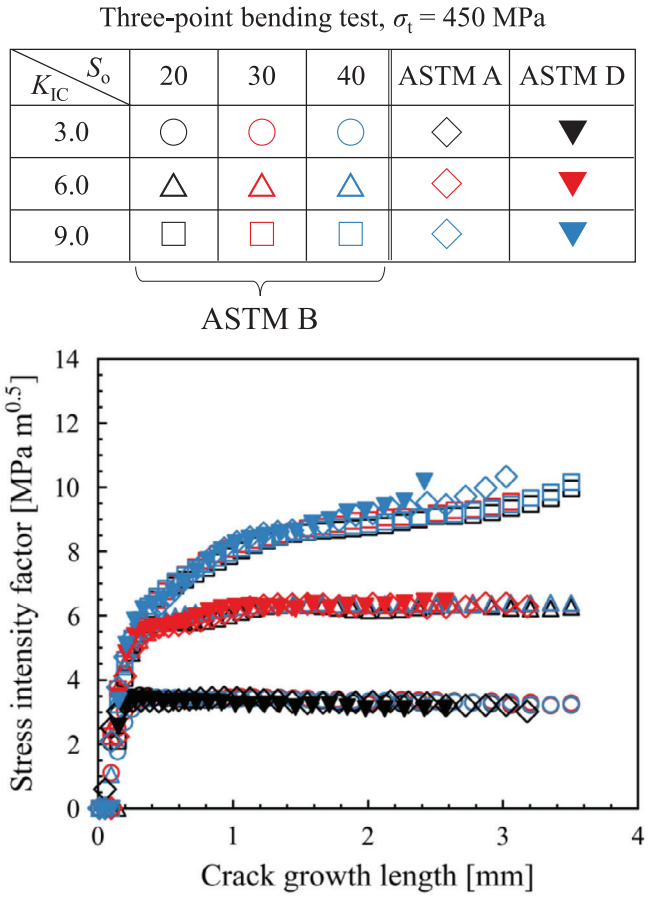

FIGURE 10 | Comparison of *R*-curve behaviors between 3PB and 4PB tests adopting fracture properties type (i). Here, the fracture toughness K_{IC} [MPa m$^{0.5}$] was varied, whereas the fracture stress (σ_t) of 450 MPa was maintained constant for all cases. ASTM, American Society for Testing and Materials.

be noted that the distribution of the local relative density of AS999 is narrow, with an average value of approximately 0.98 [32]. Hence, the microstructure of AS999 is standard dense alumina and cannot be a variable in the crack propagation in chevron-notched specimens. The specimen for the 3PB test was fabricated and machined by duplicating the ASTM B geometries (Table 1); however, the geometry deviated slightly from the standard owing to machining accuracy issues. Figure 11a,b shows close-up views around the chevron notch area (an enlarged view of "C" in Figure 12b) and the fractured surface of ASTM B specimen, respectively. A 3PB test for the ASTM B specimen under S_o = 40 mm was conducted.

Figure 12a,b shows the experimental apparatus and specimen setup, respectively. The experimental setup comprised a bending testing machine (AG-X plus, 10 kN, Shimadzu Corporation, Japan), a digital microscope (VHX-6000, Keyence Corporation, Japan), and two microphones. Two microphones were attached to both ends of the specimen with rubber bands to fix them (Figure 12b). The sounds detected by the microphones were amplified by a preamplifier and analyzed for acoustic emission (AE) using continuous-wave memory [55], which was the original AE analysis equipment. To evaluate the stable crack

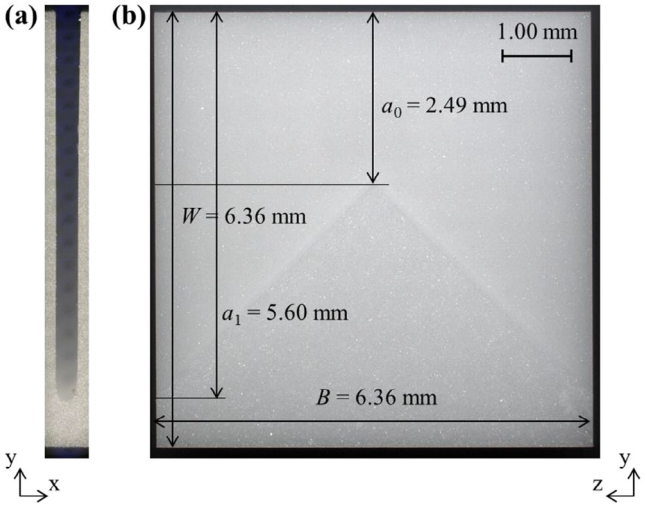

FIGURE 11 | ASTM B specimen model for 3PB test experiment showing (a) a close-up view around the chevron notch, an enlarged view of "C" in Figure 12b; (b) the fractured surface.

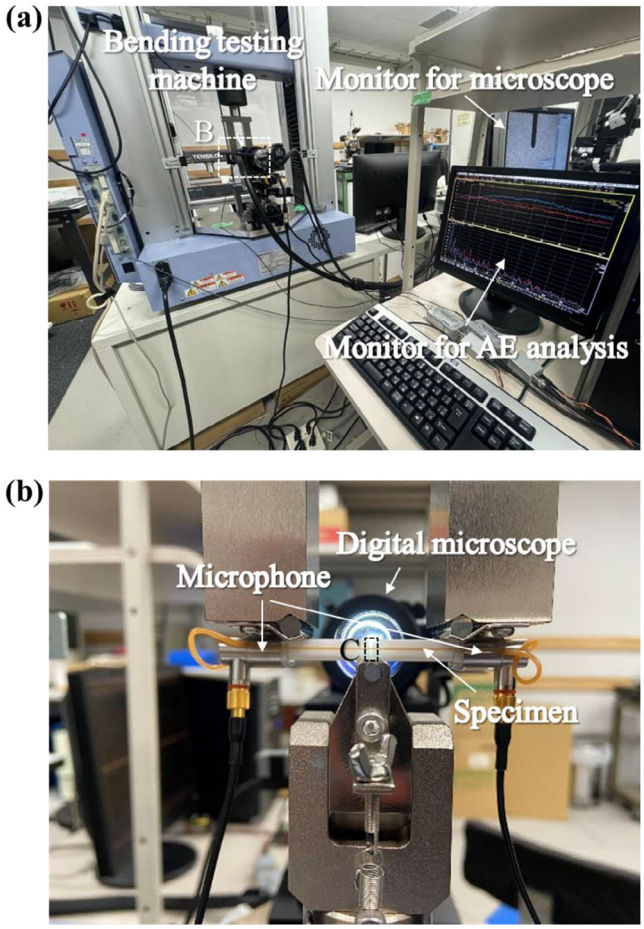

FIGURE 12 | Experimental setup for 3PB test: (a) overall view with bending testing machine, digital microscope with monitor, and AE device with monitor; (b) setting of the experimental specimen, an enlarged view of "B" in (a).

growth, a single-3PB test was performed at a crosshead speed of 0.001 mm/min at room temperature. In addition, the pre-crack area (Figure 11) was photographed at 15 s intervals, the shortest interval possible with the equipment function using a digital microscope. The images were used to measure the CMOD using DIC analysis software (VIC-2D, Laser Measurement Co. Ltd., Japan).

5.2 | Results and Discussion

Directly evaluating the *R*-curve behavior from the results of the 3PB tests using the ASTM B specimen is impossible owing to the invisibility of crack growth under the above experimental setup. Therefore, using the FEA results corresponding to the specimen used in the experiment with fracture properties of AS999, we attempted to evaluate the evolution of SIF with crack growth. Then, the occurrence of stable crack growth was determined. The geometry of the specimen in the FEA reproduced that shown in Figure 11.

As mentioned previously, in the present FEA approach, two fracture parameters (local fracture stress, σ_t, and fracture toughness, K_{IC}) are crucial to analyze the fracture and *R*-curve behavior of ceramics. For the comparison, σ_t = 544 MPa and K_{IC} = 3.4, 3.5, and 3.7 MPa $m^{0.5}$ of AS999 were used. Here, as the bulk strength of ceramics showed scatter, AE analysis was used to detect the force at the crack initiation of the target specimen during the 3PB test, and the local fracture stress σ_t was determined in an inverse analytical manner. The K_{IC} values were obtained from single-edge notched beam (SENB) tests conducted on 20 specimens of the same lot material. Ten specimens were tested at a span length of 30 mm, and the remaining 10 specimens were tested at 18 mm. The three levels of measured fracture toughness values, K_{IC} = 3.4, 3.5, and 3.7 MPa $m^{0.5}$, correspond to the lower, average, and upper limits, respectively.

First, a comparison with the experimental results is discussed. Figure 13a illustrates the force–CMOD relationship for the ASTM B specimen at S_o = 40 mm. The peak force from the FEA using the upper and lower K_{IC} was slightly higher and lower than that of the experiment, respectively; the average K_{IC} showed better agreement with the experiment. More importantly, under these test conditions, even after crack initiation, the force increased gradually with the CMOD. Furthermore, after the peak, the force decreased stably with the CMOD, indicating stable crack growth. Interestingly, in both the FEA and experiment, after crack initiation and peak force, the changes in the reaction force with the CMOD were progressive and stable. This confirmed a stable crack growth under this test condition. The present FEA approach using the continuum damage model confirmed that the fracture behavior after the peak force could be appropriately predicted.

Additionally, Figure 13b shows the variation in crack growth length with the CMOD obtained from the FEA results. Even after crack initiation and peak force, the crack growth length with the CMOD increased progressively and stably. This confirmed a stable crack growth under the test conditions. The crack growth was observed to increase up to CMOD ≈12 μm and reached a length of ~3.5 mm into the chevron notch.

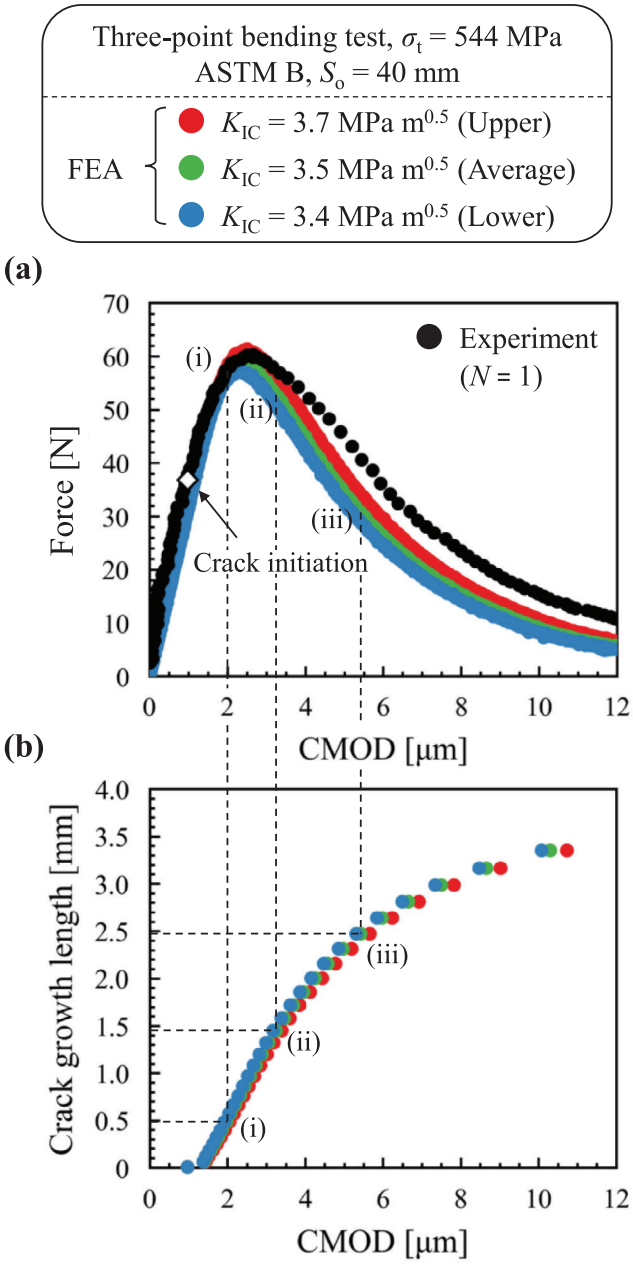

FIGURE 13 | Comparison between experimental and FEA results using the ASTM B specimen under outer span length, S_o = 40 mm: (a) force–CMOD relationships; (b) CMOD–crack growth length relationships. Here, FEAs were conducted by maintaining the fracture stress constant at σ_t = 544 MPa with the variation of fracture toughness (lower limit, average, and upper limit). ASTM, American Society for Testing and Materials; CMOD, crack mouth opening displacement.

Figure 14 shows the *R*-curve behavior of AS999 obtained from FEA and the compliance-based method. The results revealed that the SIF increased with the crack growth and eventually converged to approximately the same values as the respective input fracture toughness after the crack reached a certain length in the chevron notch. In addition to this result, the consistency of the force–CMOD relationship (Figure 13a) supported the effectiveness of the present FEA approach for evaluating the *R*-curve behavior of ceramics. Therefore, the detailed *R*-curve behavior can be evaluated simultaneously using experimental

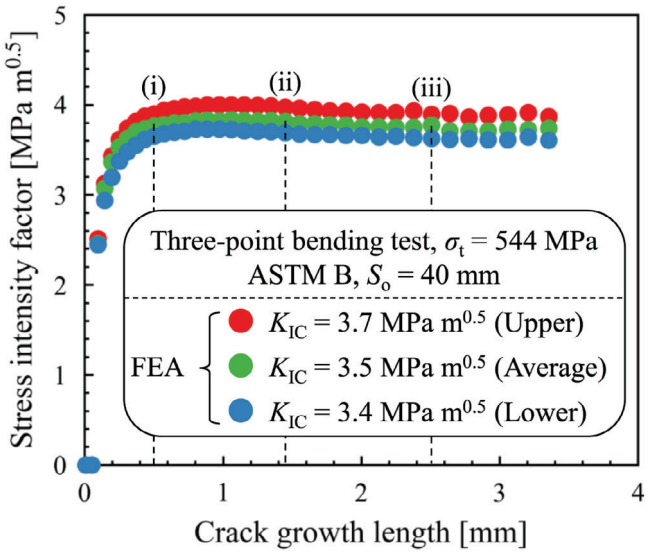

FIGURE 14 | Variation in stress intensity factor with crack growth length using the ASTM B specimen under outer span length, $S_o = 40$ mm. Here, FEAs were conducted by maintaining the fracture stress constant at $\sigma_t = 544$ MPa and varying the fracture toughness (lower limit, average, and upper limit). ASTM, American Society for Testing and Materials.

and FEA results, even with experimental systems in which crack propagation cannot be measured owing to certain limitations. Furthermore, as the *R*-curve behavior almost converged to input fracture toughness values, the experimental crack growth behavior was also reasonably estimated using the FEA approach (Figure 13b).

One of the features of FEA is the visualization of the stress and strain fields and the distribution of the state variables. Figure 15 shows the contour plots of the maximum principal stress and damage variable *D* at Part (III) (Figure 2c) corresponding to the three crack growth processes during the 3PB test with an average K_{IC}. Figure 15a–c corresponds to crack growth lengths of approximately 0.5, 1.5, and 2.5 mm, respectively ((i), (ii), and (iii) in Figures 13 and 14). The figure confirms that the crack gradually propagated from the tip of the chevron notch at the center of the specimen in the width direction to the bottom side. High maximum principal stresses were constantly applied at the crack tip, and the change in damage variable *D* corresponded to it, resulting in the reproduction of stable crack growth.

Hence, the present FEA approach overcomes the limitation of measuring the crack growth in ASTM chevron-notched specimens. Furthermore, by fitting the fracture parameters required for FEA analysis, it can be connected not only to the evaluation of fracture behaviors but also to the feasibility study of stable crack growth of the same ceramics under arbitrary boundary conditions. Another application involves evaluating the performance of self-healing ceramics. For example, when evaluating the repeated healing performance of self-healing ceramics, introducing millimeter-sized cracks stably and repeatedly is necessary. Osada et al. [39] experimentally analyzed bone-like MAX-phase self-healing ceramics using a wedge-splitting test. In such cases, the FEA approach can be applied to the feasibility of stable crack

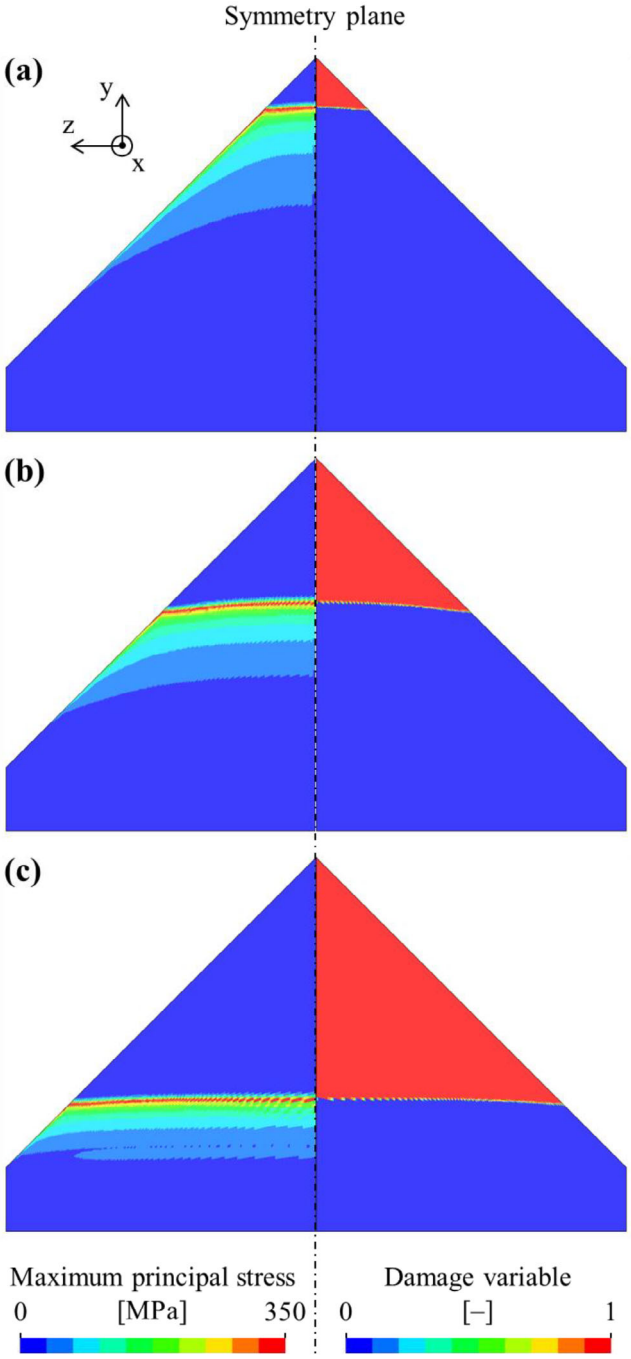

FIGURE 15 | Contour plots of the maximum principal stress and damage variable *D* at Part (III) in Figure 2c corresponding to three crack growth processes during the 3PB test with average K_{IC}. (a)–(c) correspond to crack growth lengths of approximately 0.5, 1.5, and 2.5 mm, respectively ((i), (ii), and (iii) in Figures 13 and 14).

growth and to evaluate the strength and toughness recovery after repeated cracking and healing.

6 | Conclusion

In this study, an FEA approach for the fracture and *R*-curve behavior of ceramics was investigated using a continuum damage model embedded with a cohesive-zone relationship. The

FEA of bending tests for chevron-notched specimens under various fracture properties and test geometries was conducted. Different boundary conditions resulted in different reaction force responses. However, for the same fracture toughness, the crack growth behavior (*R*-curves) was consistent regardless of the test conditions, and the output SIF of mode I converged to the input fracture toughness values as the cracks propagated. Furthermore, the 3PB test results for the chevron-notched AS999 specimens were compared with the FEA results. The overall agreement revealed that the force-CMOD-crack growth length relationships under diverse test conditions can be predicted by fitting the required fracture parameters, even with systems in which experimental measurements related to the *R*-curve and stable crack growth behavior are difficult.

It is important to note that the present damage model was formulated on the basis of cohesive zone embedded modeling, combined with a regularization technique applied to the stress–strain curve. As a result, the model's response during crack propagation within a single element is independent of the FEA mesh density. However, the damage initiation criterion is based on the maximum principal stress, which is sensitive to mesh density in regions of the stress concentration. Consequently, similar to conventional FEA, the influence of stress concentration on damage initiation exhibits slight dependence on crack length. We believe that if an FEA model is prepared to accurately capture stress gradients consistent with experimental results, the present analysis approach can reasonably simulate crack progression, regardless of mesh density and boundary conditions.

Collectively, the systematic investigation, including the comparison between FEA and experiment, supported the effectiveness of the present approach for evaluating the fracture and *R*-curve behavior of ceramics under arbitrary boundary conditions. By using the present FEA approach combined with the experiment, we can evaluate the *R*-curve behavior in detail, even with systems in which experimental measurements related to stable crack growth behavior are difficult. Furthermore, the present FEA approach can also be applied to feasibility studies on stable crack growth in actual components to ensure reliability under service conditions.

Acknowledgments

We would like to thank Dr. Kenta Goto, Dr. Hideaki Nishikawa, Dr. Hisashi Yamawaki, and Mr. Takuma Kohata at the National Institute for Materials Science (NIMS) for their support in the system development, AE analysis, and microstructural observations. Acknowledgement also goes to Mr. Hayato Ono and Mr. Haruki Okuma, Graduate School of Engineering Science, Yokohama National University, for their efforts to develop the FEA model and Python program and to measure the fracture toughness value of AS999.

References

1. H. Ohnabe, S. Masaki, M. Onozuka, K. Miyahara, and T. Sasa, "Potential Application of Ceramic Matrix Composites to Aero-Engine Components," *Composites Part A: Applied Science and Manufacturing* 30, no. 4 (1999): 489–496, https://doi.org/10.1016/S1359-835X(98)00139-0.

2. K. N. Lee, "Current Status of Environmental Barrier Coatings for Si-Based Ceramics," *Surface & Coatings Technology* 133 (2000): 1–7, https://doi.org/10.1016/S0257-8972(00)00889-6.

3. A. N. Samant and N. B. Dahotre, "Laser Machining of Structural Ceramics-A Review," *Journal of the European Ceramic Society* 29, no. 6 (2009): 969–993, https://doi.org/10.1016/j.jeurceramsoc.2008.11.010.

4. O. Gavalda Diaz, G. Garcia Luna, Z. Liao, and D. Axinte, "The New Challenges of Machining Ceramic Matrix Composites (CMCs): Review of Surface Integrity," *International Journal of Machine Tools and Manufacture* 139 (2019): 24–36, https://doi.org/10.1016/j.ijmachtools.2019.01.003.

5. S. R. Levine, E. J. Opila, M. C. Halbig, J. D. Kiser, M. Singh, and J. A. Salem, "Evaluation of Ultra-High Temperature Ceramics Foraeropropulsion Use," *Journal of the European Ceramic Society* 22, no. 14–15 (2002): 2757–2767, https://doi.org/10.1016/S0955-2219(02)00140-1.

6. Z. Zhao, L. Zhang, J. Zheng, H. Bai, S. Zhang, and B. Xu, "Microstructures and Mechanical Properties of Al_2O_3/ZrO_2 Composite Produced by Combustion Synthesis," *Scripta Materialia* 53, no. 8 (2005): 995–1000, https://doi.org/10.1016/j.scriptamat.2005.06.016.

7. N. P. Padture, "Advanced Structural Ceramics in Aerospace Propulsion," *Nature Materials* 15, no. 8 (2016): 804–809, https://doi.org/10.1038/nmat4687.

8. G. Zhu, Q. Feng, J. Yang, et al., "Effect of BNNTs/Matrix Interface Tailoring on Toughness and Fracture Morphology of Hierarchical SiCf/SiC Composites," *Journal of Advanced Ceramics* 8, no. 4 (2019): 555–563, https://doi.org/10.1007/s40145-019-0338-0.

9. D. Li, P. Jiang, R. Gao, F. Sun, X. Jin, and X. Fan, "Experimental and Numerical Investigation on the Thermal and Mechanical Behaviours of Thermal Barrier Coatings Exposed to CMAS Corrosion," *Journal of Advanced Ceramics* 10, no. 3 (2021): 551–564, https://doi.org/10.1007/s40145-021-0457-2.

10. Z. Liu, S. Zhao, T. Yang, and J. Zhou, "Improvement in Mechanical Properties in AlN-h-BN Composites With High Thermal Conductivity," *Journal of Advanced Ceramics* 10, no. 6 (2021): 1317–1325, https://doi.org/10.1007/s40145-021-0506-0.

11. L. Yu, H. Liu, Y. Fu, et al., "Design and Preparation of an Ultra-High Temperature Ceramic by In-Situ Introduction of $Zr_2[Al(Si)]_4C_5$ Into ZrB_2-SiC: Investigation on the Mechanical Properties and Oxidation Behavior," *Journal of Advanced Ceramics* 10, no. 5 (2021): 1082–1094, https://doi.org/10.1007/s40145-021-0493-y.

12. A. G. Evans, L. R. Russell, and D. W. Richerson, "Slow Crack Growth in Ceramic Materials at Elevated Temperatures," *Metallurgical Transactions A* 6 (1975): 707–716.

13. I. Tanaka and G. Pezzotti, "Evaluation of Slow Crack Growth Resistance in Ceramics for High-Temperature Applications," *Journal of the American Ceramic Society* 75, no. 4 (1992): 772–777, https://doi.org/10.1111/j.1151-2916.1992.tb04140.x.

14. C. C. Gonzaga, P. F. Cesar, W. G. Miranda, and H. N. Yoshimura, "Slow Crack Growth and Reliability of Dental Ceramics," *Dental Materials* 27, no. 4 (2011): 394–406, https://doi.org/10.1016/j.dental.2010.10.025.

15. K. Takahashi, M. Yokouchi, S.-K. Lee, and K. Ando, "Development of Structural Ceramics Having Large Crack-Healing Ability and Fracture Toughness," *Smart Materials III* 5648 (2004): 276–283, https://doi.org/10.1117/12.580719.

16. L. Sestakova, R. Bermejo, Z. Chlup, and R. Danzer, "Strategies for Fracture Toughness, Strength and Reliability Optimisation of Ceramic-Ceramic Laminates," *International Journal of Materials Research* 102, no. 6 (2011): 613–626, https://doi.org/10.3139/146.110523.

17. R. W. Steinbrech, "*R*-Curve Behavior of Ceramics," *Fracture Mechanics of Ceramics: Composites, R-Curve Behavior, and Fatigue* 9 (1992): 187–208.

18. S. Kovalev, T. Miyajima, Y. Yamauchi, and M. Sakai, "Numerical Evaluation of Toughening by Crack-Face Grain Interlocking in Self-

Reinforced Ceramics," *Journal of the American Ceramic Society* 83, no. 4 (2000): 817–824, https://doi.org/10.1111/j.1151-2916.2000.tb01280.x.

19. P. F. Becher, "Microstructural Design of Toughened Ceramics," *Journal of the American Ceramic Society* 74, no. 2 (1991): 255–269, https://doi.org/10.1111/j.1151-2916.1991.tb06872.x.

20. P. F. Becher, "Advances in the Design of Toughened Ceramics," *Journal of the Ceramic Society of Japan* 99, no. 1154 (1991): 993–1001.

21. S. J. Grutzik, S. Dai, and K. T. Strong. "Investigation of R-Curve Behavior in Glass Ceramic Materials," EE LDRD Project #214906, SAND2019-11503 (2019): 1–33.

22. M. Kurumatani, K. Terada, J. Kato, T. Kyoya, and K. Kashiyama, "An Isotropic Damage Model Based on Fracture Mechanics for Concrete," *Engineering Fracture Mechanics* 155 (2016): 49–66, https://doi.org/10.1016/j.engfracmech.2016.01.020.

23. S. Ozaki, M. Nakamura, and T. Osada, "Finite Element Analysis of the Fracture Statistics of Self-Healing Ceramics," *Science and Technology of Advanced Materials* 21, no. 1 (2020): 609–625, https://doi.org/10.1080/14686996.2020.1800368.

24. S. Ozaki, J. Yamamoto, N. Kanda, and T. Osada, "Kinetics-Based Constitutive Model for Self-Healing Ceramics and Its Application to Finite Element Analysis of Alumina/SiC Composites," *Open Ceramics* 6 (2021): 100135, https://doi.org/10.1016/j.oceram.2021.100135.

25. T. Maeda, T. Osada, and S. Ozaki, "Novel Numerical Approach for Reliability-Assurance of Ceramics by Combining Self-Crack-Healing With Proof Testing," *Journal of the European Ceramic Society* 44, no. 4 (2024): 2261–2270, https://doi.org/10.1016/j.jeurceramsoc.2023.10.077.

26. J. Oliver, "A Consistent Characteristic Length for Smeared Cracking Models," *International Journal for Numerical Methods in Engineering* 28, no. 2 (1989): 461–474, https://doi.org/10.1002/nme.1620280214.

27. ASTM International. *Standard Test Methods for Determination of Fracture Toughness of Advanced Ceramics at Ambient Temperature*, C1421-01b (ASTM International, 2002).

28. ANSYS . *LS-DYNA User's Manual* (ANSYS, 2021).

29. T. Osada, T. Hara, M. Mitome, et al., "Self-Healing by Design: Universal Kinetic Model of Strength Recovery in Self-Healing Ceramics," *Science and Technology of Advanced Materials* 21 (2020): 593–608, https://doi.org/10.1080/14686996.2020.1796468.

30. K. Takahashi, M. Yokouchi, S. K. Lee, and K. Ando, "Crack-Healing Behavior of Al_2O_3 Toughened by SiC Whiskers," *Journal of the American Ceramic Society* 86, no. 12 (2003): 2143–2147, https://doi.org/10.1111/j.1151-2916.2003.tb03622.x.

31. F. Bouville, E. Maire, S. Meille, B. van de Moortèle, A. J. Stevenson, and S. Deville, "Strong, Tough and Stiff Bioinspired Ceramics From Brittle Constituents," *Nature Materials* 13, no. 5 (2014): 508–514, https://doi.org/10.1038/nmat3915.

32. C. Ito, T. Maeda, R. Higashi, T. Osada, T. Kohata, and S. Ozaki, "Application of Extreme Value Statistics to Internal Pore Distribution in Ceramics and Prediction of Size Dependency of Strength Scatter," *Journal of the European Ceramic Society* 44, no. 5 (2024): 3381–3392, https://doi.org/10.1016/j.jeurceramsoc.2023.12.021.

33. J. Pittari, G. Subhash, J. Zheng, V. Halls, and P. Jannotti, "The Rate-Dependent Fracture Toughness of Silicon Carbide- and Boron Carbide-Based Ceramics," *Journal of the European Ceramic Society* 35, no. 16 (2015): 4411–4422, https://doi.org/10.1016/j.jeurceramsoc.2015.08.027.

34. D. Munz, R. T. Bubsey, and J. L. Shannon, "Fracture Toughness Determination of Al_2O_3 Using Four-Point-Bend Specimens With Straight-Through and Chevron Notches," *Journal of the American Ceramic Society* 63, no. 5–6 (1980): 300–305.

35. A. D. Bakker, "Evaluation of Elastic Fracture Mechanics Parameters for Bend Specimens," *International Journal of Fracture* 71 (1995): 323–343, https://doi.org/10.1007/BF00037813.

36. T. L. Anderson, *Fracture Mechanics: Fundamentals and Applications* (CRC Press, 2005).

37. M. E. Ebrahimi, J. Chevalier, and G. Fantozzi, "*R*-Curve Evaluation and Bridging Stress Determination in Alumina by Compliance Analysis," *Journal of the European Ceramic Society* 23, no. 6 (2003): 943–949.

38. Y. Huang and W. Zhou, "Numerical Investigation of Compliance Equations Used in the *R*-Curve Testing for Clamped SE (T) Specimens," *Fatigue and Fracture of Engineering Materials and Structures* 38, no. 10 (2015): 1137–1154, https://doi.org/10.1111/ffe.12293.

39. T. Osada, A. Watabe, J. Yamamoto, et al., "Full Strength and Toughness Recovery After Repeated Cracking and Healing in Bone-Like High Temperature Ceramics," *Scientific Reports* 10, no. 1 (2020): 18990, https://doi.org/10.1038/s41598-020-75552-1.

40. A. Bornhauser, K. Kromp, and R. F. Pabst, "*R*-Curve Evaluation With Ceramic Materials at Elevated Temperatures by an Energy Approach Using Direct Observation and Compliance Calculation of the Crack Length," *Journal of Materials Science* 20 (1985): 2586–2596.

41. Y.-W. Mai, X. Hu, K. Duan, and B. Cotterell, "Crack-Resistance Curve and Cyclic Fatigue in Ceramic Materials," in *Fracture Mechanics of Ceramics: Composites, R-Curve Behavior, and Fatigue*, ed. R. C. Bradt, D. P. H. Hasselman, D. Munz, M. Sakai, and V. Y. Shevchenko (Springer, 1992), 387–422.

42. W. Zhang, R. Telle, and J. Uebel, "*R*-Curve Behaviour in Weak Interface-Toughened SiC-C Laminates by Discrete Element Modelling," *Journal of the European Ceramic Society* 34, no. 2 (2014): 217–227, https://doi.org/10.1016/j.jeurceramsoc.2013.08.021.

43. C. López-Pernía, C. Muñoz-Ferreiro, J. Prada-Rodrigo, et al., "*R*-Curve Evaluation of 3YTZP/Graphene Composites by Indirect Compliance Method," *Journal of the European Ceramic Society* 43, no. 8 (2023): 3486–3497, https://doi.org/10.1016/j.jeurceramsoc.2023.02.002.

44. D. Bleise and R. W. Steinbrech, "Flat *R*-Curve From Stable Propagation of Indentation Cracks in Coarse-Grained Alumina," *Journal of the American Ceramic Society* 77, no. 2 (1994): 315–322, https://doi.org/10.1111/j.1151-2916.1994.tb06998.x.

45. N. Ramachandran and D. K. Shetty, "Rising Crack-Growth-Resistance (*R*-Curve) Behavior of Toughened Alumina and Silicon Nitride," *Journal of the American Ceramic Society* 74, no. 10 (1991): 2634–2641, https://doi.org/10.1111/j.1151-2916.1991.tb06812.x.

46. T. Nishida, Y. Hanaki, T. Nojima, and G. Pezzotti, "Measurement of Rising *R*-Curve Behavior in Toughened Silicon Nitride by Stable Crack Propagation in Bending," *Journal of the American Ceramic Society* 78, no. 11 (1995): 3113–3116, https://doi.org/10.1111/j.1151-2916.1995.tb09092.x.

47. Q. L. Feng, F. Z. Cui, G. Pu, R. Z. Wang, and H. D. Li, "Crystal Orientation, Toughening Mechanisms and a Mimic of Nacre," *Materials Science and Engineering C* 11, no. 1 (2000): 19–25.

48. F. Song, A. K. Soh, and Y. L. Bai, "Structural and Mechanical Properties of the Organic Matrix Layers of Nacre," *Biomaterials* 24, no. 20 (2003): 3623–3631, https://doi.org/10.1016/S0142-9612(03)00215-1.

49. G. Yamamoto, M. Omori, T. Hashida, and H. Kimura, "A Novel Structure for Carbon Nanotube Reinforced Alumina Composites With Improved Mechanical Properties," *Nanotechnology* 19, no. 31 (2008): 315708, https://doi.org/10.1088/0957-4484/19/31/315708.

50. M. E. Launey, E. Munch, D. H. Alsem, et al., "Designing Highly Toughened Hybrid Composites Through Nature-Inspired Hierarchical Complexity," *Acta Materialia* 57, no. 10 (2009): 2919–2932, https://doi.org/10.1016/j.actamat.2009.03.003.

51. M. E. Launey, E. Munch, D. H. Alsem, E. Saiz, A. P. Tomsia, and R. O. Ritchie, "A Novel Biomimetic Approach to the Design of High-Performance Ceramic–Metal Composites," *Journal of the Royal Society, Interface* 7, no. 46 (2010): 741–753, https://doi.org/10.1098/rsif.2009.0331.

52. J. Liu, H. Yan, and K. Jiang, "Mechanical Properties of Graphene Platelet-Reinforced Alumina Ceramic Composites," *Ceramics Interna-*

tional 39, no. 6 (2013): 6215–6221, https://doi.org/10.1016/j.ceramint.2013.01.041.

53. R. Pavlacka, R. Bermejo, Y. Chang, D. J. Green, and G. L. Messing, "Fracture Behavior of Layered Alumina Microstructural Composites With Highly Textured Layers," *Journal of the American Ceramic Society* 96, no. 5 (2013): 1577–1585, https://doi.org/10.1111/jace.12292.

54. M. Lugovy, N. Orlovskaya, M. Neumann, et al., "Room Temperature *R*-Curve and Stable Crack Growth Behaviour of ZrB_2–SiC Ceramic Composites," *Advances in Applied Ceramics* 118, no. 4 (2019): 169–182, https://doi.org/10.1080/17436753.2018.1471443.

55. K. Ito and M. Enoki, "Acquisition and Analysis of Continuous Acoustic Emission Waveform for Classification of Damage Sources in Ceramic Fiber Mat," *Materials Transactions* 48, no. 6 (2007): 1221–1226, https://doi.org/10.2320/matertrans.I-MRA2007850.